

PAPER • OPEN ACCESS

Single harmonic-based narrowband magnetic particle imaging

To cite this article: Klaas-Julian Janssen *et al* 2022 *Meas. Sci. Technol.* **33** 095405

View the [article online](#) for updates and enhancements.

You may also like

- [Magnetic particle spectroscopy-based bioassays: methods, applications, advances, and future opportunities](#)
Kai Wu, Diqing Su, Renata Saha et al.
- [Increasing the sensitivity for stem cell monitoring in system-function based magnetic particle imaging](#)
Kolja Them, J Salamon, P Szwargulski et al.
- [A study on influence of superparamagnetic iron oxide nanoparticles \(SPIONs\) on green gram \(*Vigna radiata* L.\) and earthworm \(*Eudrilus eugeniae* L.\)](#)
Antony V Samrot, SaiPriya C, Jenifer Selvarani A et al.

Single harmonic-based narrowband magnetic particle imaging

Klaas-Julian Janssen¹ , Meinhard Schilling¹, Frank Ludwig¹ and Jing Zhong^{1,2,*} 

¹ Institut für Elektrische Messtechnik und Grundlagen der Elektrotechnik, TU Braunschweig, Braunschweig, Germany

² School of Instrumentation and Optoelectronic Engineering, Beihang University, Beijing, People's Republic of China

E-mail: j.zhong@tu-braunschweig.de

Received 26 January 2022, revised 1 June 2022

Accepted for publication 14 June 2022

Published 24 June 2022



CrossMark

Abstract

Magnetic particle imaging (MPI) quantitatively visualizes *in vivo* superparamagnetic iron oxide nanoparticles (SPIONs), which has shown great promises in biomedicine. In this paper, we propose a single harmonic-based narrowband MPI approach via measuring a single harmonic— $3f_0$ harmonic—of the SPIONs induced in an excitation magnetic field with frequency $f_0 = 5$ kHz. The narrowband MPI scanner is built to scan the field-free-point, generated by a pair of permanent magnets, through an imaging field-of-view, and to measure the magnetic response of the SPIONs by a narrowband receive system. The narrowband MPI approach dramatically reduces the design efforts in the transmit system and noise matching in the receive system. Phantom experiments are performed with the custom-built narrowband MPI scanner to evaluate the spatial resolution and limit of detection (LOD). Experimental results indicate that the proposed single harmonic-based narrowband MPI approach allows a spatial resolution of 0.5 mm and an LOD of $27 \mu\text{g (Fe) ml}^{-1}$ (254 ng Fe weight) using Perimag[®] SPIONs, which can significantly be improved by using optimized SPIONs and by improving the detection circuitry. We believe that the proposed narrowband MPI approach minimizes the MPI hardware efforts but still allows for good performance in terms of spatial resolution and LOD.

Supplementary material for this article is available [online](#)

Keywords: magnetic particle imaging, superparamagnetic iron oxide nanoparticles, single harmonic, spatial resolution, limit of detection

(Some figures may appear in colour only in the online journal)

1. Introduction

Superparamagnetic iron oxide nanoparticles (SPIONs) have shown great promise as an emerging platform in disease

diagnostics and therapy. For instance, SPIONs functionalized with antibodies bind to their specific antigens, allowing the tracking and imaging of the antigens for disease diagnostics [1–4]. In targeted drug delivery, SPIONs together with drugs encapsulated into polymers are used as magnetic carriers for targeting specific tissue with external gradient magnetic fields to improve treatment efficiency [5–7]. In addition, the SPIONs are also used as heaters when applying radio-frequency ac magnetic fields to release the drugs from the polymers [8–11]. In cell-based cancer therapy, e.g. adoptive cellular therapy, the labeling of SPIONs onto the surface of specific

* Author to whom any correspondence should be addressed.



Original content from this work may be used under the terms of the [Creative Commons Attribution 4.0 licence](#). Any further distribution of this work must maintain attribution to the author(s) and the title of the work, journal citation and DOI.

cells allows *in vivo* tracking [12–16]. For all these applications, a novel imaging modality for the SPION imaging provides new insights into the development of new techniques for disease diagnostics and therapy.

Magnetic particle imaging (MPI) is a novel imaging modality, which directly measures the nonlinear magnetic response of SPIONs for *in vivo* quantification and imaging of the SPIONs [17, 18]. In 2005, the MPI technique was for the first time reported by Gleich and Weizenecker, demonstrating the feasibility of MPI for SPION imaging [17]. The spectra of magnetic response of the SPIONs exposed in magnetic fields were measured for imaging with system matrix-based reconstruction based on scanning field-free-point (FFP) in a field-of-view (FOV). Since then, there have been various MPI approaches, differing in imaging methodology and scanner design. In 2009, Goodwill *et al* proposed the *x*-space MPI approach by calculating the FFP position and the SPION magnetization in time-domain, which in principle allows SPION imaging by gridding the time-domain SPION magnetization without a system matrix-based reconstruction [19–21]. In 2014, Vogel *et al* developed an alternative approach of MPI, named traveling-wave MPI, without using permanent magnets [22]. In addition, single-sided MPI was developed to solve the problem of a size limitation for the specimens [23, 24] while field-free-line (FFL)-based MPI approaches were also developed to improve the signal-to-noise ratio (SNR) [20, 25, 26].

To date, MPI has been demonstrated to allow three-dimensional (3D) and real-time imaging of SPIONs with high sensitivity and high spatial resolution. In 2009, Weizenecker *et al* demonstrated that MPI allowed 3D and real-time imaging of the SPIONs with 46 frames per second (FPS) and a spatial resolution of about 1 mm [27]. In 2020, Vogel *et al* reported on a 2000 FPS-superspeed bolus visualization with traveling-wave MPI [28]. The spatial resolution of MPI depends on several factors, including the gradient magnetic field, the magnetic properties of SPIONs and the drive field (DF). For system matrix-based MPI, a spatial resolution of about 0.5 mm was reported with a gradient of 2 T m⁻¹ [29] whereas for *x*-space MPI a spatial resolution of 0.6 mm was estimated with a gradient of 6 T m⁻¹ [30]. In 2019, Tay *et al* reported on pulsed-excitation MPI, improving the spatial resolution of *x*-space MPI to better than 0.5 mm with gradient 7 T m⁻¹ [31]. In 2021, Tay *et al* further improved the spatial resolution of MPI to 0.15 mm with gradient of 6.3 T m⁻¹ by using super-ferromagnetic iron oxide nanoparticle chains [32]. In principle, MPI allows a better sensitivity than MRI by an order of 3–6 by considering the magnetic moments of SPIONs and hydrogen, as well as the excitation frequency [33]. To date, the best limit of detection (LOD) of 5 ng iron achieved by MPI was reported by Gräser *et al* with an acquisition time of 2.14 s by integrating a new gradiometric detection coil and improving the pre-amplifier in the commercial MPI scanner from Bruker [34]. In a general broadband MPI scanner, a DF with a large amplitude and high frequency is applied to simultaneously scan the FFP and excite the SPIONs. To allow a larger FOV, either the DF strength should be increased or an

additional focus field should be applied to move the FFP/FFL. Thus, these general broadband MPI scanners employ DFs with frequency of a few tens of kHz and tens of mT while a detection system with a measurement bandwidth of about hundreds of kHz (even MHz). However, a higher DF may cause significant concerns in human safety due to magnetostimulation [35]. In addition, previous studies demonstrated that a lower DF strength may lead to a better spatial resolution [36, 37]. For the system matrix-based MPI approaches, the system matrix should be measured by mechanically scanning a spot sample in the FOV, which is very time-consuming—in the order of tens of hours, depending on the averaging times and the FOV.

In addition to these general MPI approaches (broadband MPI approaches), the approaches of narrowband MPI have been reported for the imaging of the SPIONs [33, 38–44]. For instance, Goodwill *et al* investigated a narrowband MPI approach by using an excitation magnetic field at 150 kHz and a modulation magnetic field at 200 Hz. The second harmonic (300 kHz) of the SPIONs was measured for imaging with a 10.3 min acquisition time for two-dimensional (2D) imaging without providing details on spatial resolution or LOD [33]. Pi *et al* developed an MPI approach via the measurements of the SPION susceptibility by measuring the fundamental harmonic at 12.8 kHz, where an LOD of 12.5 µg and a spatial resolution of about 2.5 mm at 4.3 T m⁻¹ were achieved [40]. The magnetic signal from tissue may contaminate the SPION signal, which leads to a limitation of the LOD. In 2019, Trisnanto *et al* reported on a narrowband MPI by modulating the relaxation response of SPIONs for submillimeter resolution [44]. In addition, other approaches using an array of magnetic sensors or mechanical scanning of a magnetic sensor or a phantom were also reported for imaging SPIONs [45–48]. In 2017, Mason *et al* presented by simulation a human brain FFL scanner by using the 3rd harmonic for the SPION imaging [49]. Afterwards, in 2021 the same group experimentally presented the approach for the SPION imaging with a spatial resolution of 2–3 mm (2.83 T m⁻¹ gradient field strength) and an LOD of 100 ng with an excitation field frequency of 25 kHz and a peak amplitude of 12 mT [50]. In 2021, Tonyushkin *et al* investigated a single sided FFL MPI approach based on the 3rd harmonic of the SPIONs by simulation and experiments. The simulated spatial resolution is about 2 mm (2 T m⁻¹ gradient field strength) [51, 52]. In principle, narrowband MPI employs a high-Q receive system, which reduces the bandwidth requirements and may improve the SNR for a given DF. To date, there have been no approaches that comprehensively investigate the spatial resolution and the LOD of narrowband MPI with measurements by varying the iron concentration and the DF strength.

In this paper, we propose an approach of single harmonic-based narrowband MPI to visualize the spatial distribution of the SPIONs. The method of spatial encoding of the SPIONs is presented while a narrowband MPI scanner is built. An one-dimensional (1D) excitation magnetic field at $f_0 = 5$ kHz is applied to excite the SPIONs while a quasi-static field is used to scan the FFP through the FOV. Only the 3rd

harmonic at 15 kHz is measured for imaging with reconstruction. The excitation magnetic field-dependent point spread functions (PSFs) are measured and discussed. Experiments on different phantoms are performed to comprehensively analyze the spatial resolution and LOD. The objective of this work is to demonstrate the feasibility of this MPI approach for SPION imaging with good imaging performance while the efforts for the design of the MPI scanner can be significantly reduced.

2. Methods

2.1. Concept

The concept of 1D single harmonic-based narrowband MPI is depicted in figure 1. In an FOV, a gradient magnetic field H_G generates an FFP, which can be moved by a scanning magnetic field H_s , as shown in figures 1(a) and (b). Scanning the FFP position x_{FFP} by H_s , the time-domain magnetization $M(t)$ of a spot SPION sample located at origin position induced by an excitation magnetic field H_{ac} with excitation frequency f_0 is modulated, as shown in figure 1(b). Note that here the FFP movement by H_{ac} is ignored. Figure 1(c) shows the schematic of $M(t)$ vs $x_{\text{FFP}}(t)$ curve in x -direction. In a short subinterval dt , the signal strength of the 3rd harmonic M_3 at frequency $3f_0$ is calculated from the time-domain SPION magnetization $M(t)$ while the FFP position x_{FFP} , considered as a constant in the subinterval dt , is calculated and scaled in x axis. Consequently, $M_3(x_{\text{FFP}})$ is obtained, which can be considered as the PSF $\text{PSF}(x)$ of the narrowband MPI in x -direction. Therefore, the measured 3rd harmonic $M_3(x)$ at the FFP position is an integration over the imaging FOV and can be written as a convolution of $h(x)$ and the PSF of the third harmonic $\text{PSF}(x)$:

$$M_3(x_{\text{FFP}}) = h(x) * \text{PSF}(x)|_{x=x_{\text{FFP}}}, \quad (1)$$

where $h(x)$ is the 3rd harmonic generated by the local SPIONs at position x . Figure 1(d) shows the schematic of 1D PSFs, $M_3(x_{\text{FFP}})$ and $M_3(z_{\text{FFP}})$, in x - and z -direction. Note that negative M_3 represents the opposite direction of the 3rd harmonic vs the excitation magnetic field. In addition, since x_{FFP} vs time t curve is not linear, the time-domain magnetization $M(t)$ depicted in figures 1(b) and (c) shows a slightly different shape at the edge. Here the excitation magnetic field is set to be parallel to the sensitive axis of a detection coil. A deconvolution or reconstruction method allows the measurement of the spatial distribution of $h(x)$ generated by local SPIONs, which is proportional to the SPION concentration. Therefore, scanning the FFP in multi-dimensions enables multi-dimensional imaging of the SPIONs.

2.2. Scanner design

According to the imaging concept, an MPI scanner was built to generate the desired magnetic fields and to measure the magnetic response of the SPIONs. Figures 2(a) and (b) show a schematic of the coil configuration and a photo of the MPI scanner, respectively.

The magnets of a former MPI scanner [48] were modified to generate the FFP and quasi-static scanning magnetic fields to move the FFP in z -direction in the FOV, as shown in figure 2(a). A pair of NdFeB permanent magnets were oppositely arranged to generate the FFP with a gradient of about 4.4 T m^{-1} in z -direction and 2.2 T m^{-1} in x - and y -directions. A Helmholtz coil pair was used to generate scanning magnetic field $\mu_0 H_s$ for the FFP movement in the z -direction. In the current status of the MPI scanner, only in z -direction the FFP is electrically moved by a scanning magnetic field. In x -direction the sample is mechanically moved through the FFP. Fully electrical scanning in x - and z -direction can be achieved by adding a coil in x -direction. Figure 2(b) shows the photo of the MPI scanner, with the robot, which is used for movement in x -direction, in front of the system. It is important to have some distance between the motor-drivers of the robot and the coil system to remove the noise of the electronic. The schematic of the analog signal chain is shown in figure 3.

The analog transmit chain of the system includes a solenoidal coil whose impedance is matched by a series and a parallel capacitor. This coil generates the excitation magnetic field $\mu_0 H_{\text{ac}}$ in x -direction (see the green coil in figure 2(a)) at 5 kHz, driven by a power amplifier (V_{ex}) A 1110-16-A, purchased from Dr Hubert (Bochum, Germany). The excitation frequency of 5 kHz is chosen to investigate the SPION spectra with significant contribution from Brownian relaxation. A 3rd-order band-pass filter was used to improve the total harmonic distortion (THD) of the excitation magnetic field. The required power in the transmit system was estimated to be about 18 W with $\mu_0 H_{\text{ac}} = 4 \text{ mT}$.

A gradiometric receive coil, including the detection and compensation coils, was used to detect the magnetic response of the SPIONs (see the inner blue coils in figure 2(a)). The gradiometric coil was wound on a resin-printed bobbin with an inner diameter (bore size) of 22 mm. In this paper, the 3rd harmonic (M_3) of the SPION signal at frequency 15 kHz was measured for imaging. To improve the SNR of the measurement signal and to suppress the feedthrough from the excitation magnetic field, a resonance circuit and a high-pass were used to tune the resonance frequency of the gradiometric coil to 15 kHz, as shown in figure 3. Afterwards, a 2nd-order band-stop filter was used to further suppress the feedthrough signal. A low-noise preamplifier based on an AD8221 instrumentation amplifier was designed to amplify the signal from the gradiometric detection coil. The output signal of the pre-amplifier is transferred to differential signals via an AD8066 in the next amplifier stage. Afterwards, the analog signal is digitalized by a National Instruments (NI) data acquisition card (NI PCIe-6374) with a sampling rate of 1 MHz for further processing, e.g. digital lock-in detection and segmentation.

Note that the current MPI scanner was built without any cooling system or shielding systems, which significantly reduced the construction effort compared to general MPI scanner. For the proposed narrowband MPI approach, the excitation magnetic field H_{ac} is used to excite the SPIONs while the scanning magnetic field is used to electrically move the FFP in the FOV. The small movement of the FFP by the excitation

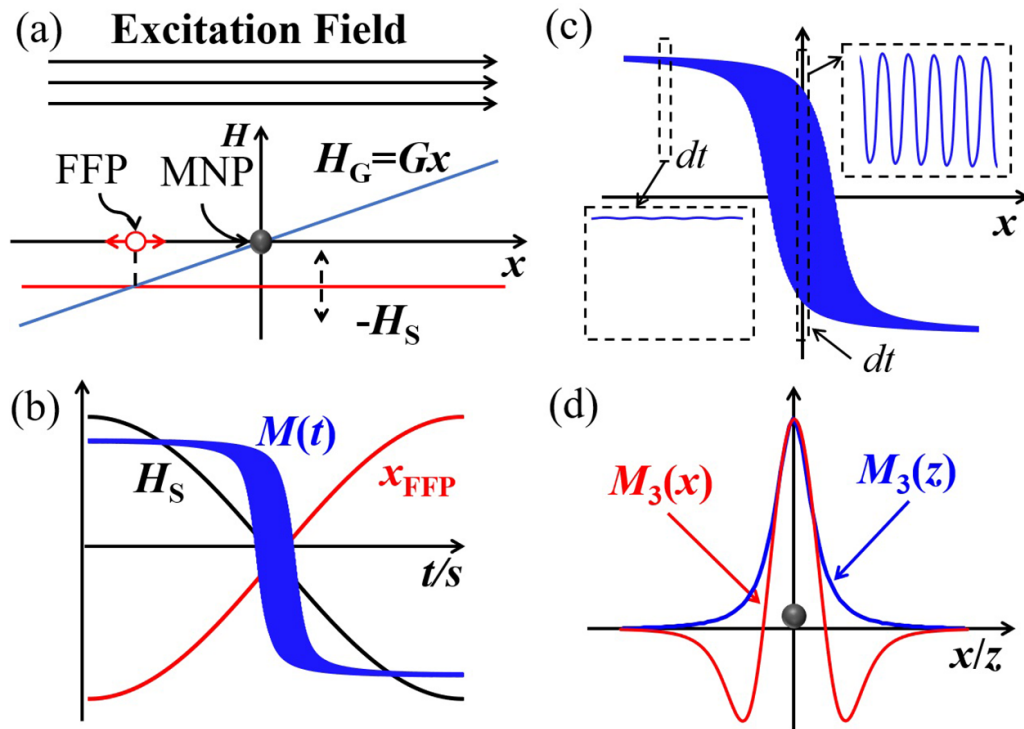


Figure 1. Imaging concept of the single harmonic-based narrowband MPI. (a) Schematic of gradient magnetic field H_G for the generation of an FFP, scanning magnetic field H_s for the FFP scanning, and excitation magnetic field H_{ac} for the SPION excitation. (b) Schematic of the scanning magnetic field $H_s(t)$, the FFP position $x_{FFP}(t)$, and the SPION magnetization $M(t)$ in time domain. (c) Schematic of the time-domain magnetization $M(t)$ vs $x_{FFP}(t)$ in x -direction. In the short subinterval dt , the signal strength of the 3rd harmonic M_3 is calculated from the time-domain SPION magnetization while the FFP position x_{FFP} , considered as a constant in the short subinterval dt , is calculated by averaging the scanning magnetic field and the given gradient magnetic field. In this case, the calculated 1D PSFs $M_3(x)$, as well as $M_3(z)$, is presented in (d).

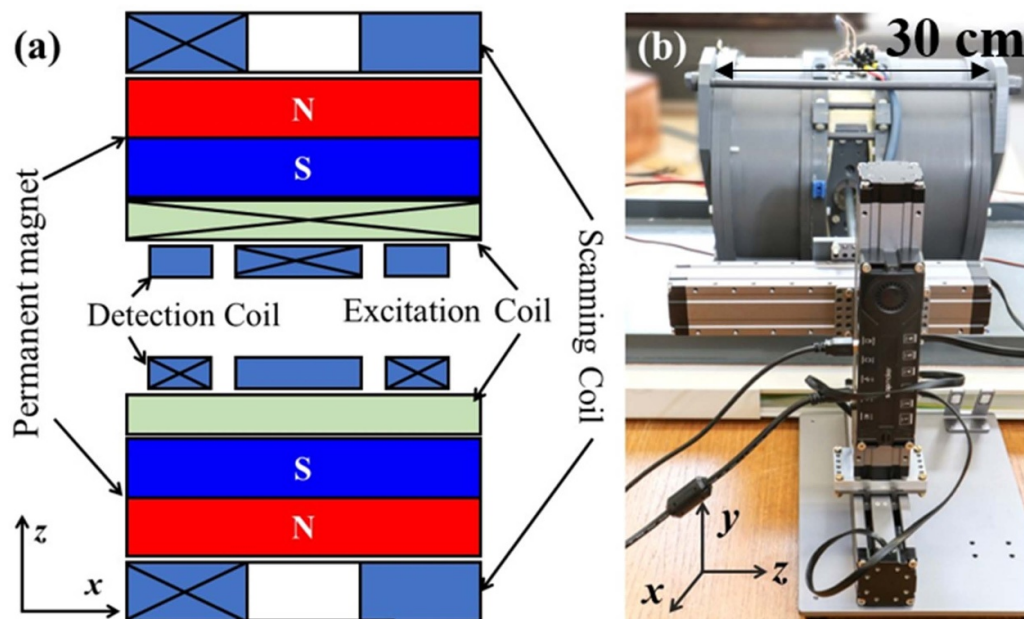


Figure 2. The overview of the narrowband MPI scanner. Figure (a) shows the schematic of the MPI scanner from top view with a slice in xz plane. The winding directions of the coils are shown with a cross. The excitation and gradiometric detection coils are placed between the two NdFeB permanent magnets. (b) Photo of the built MPI scanner.

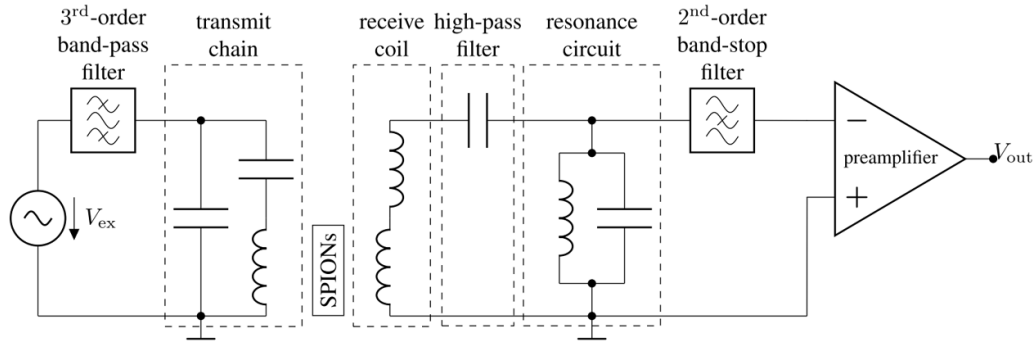


Figure 3. Schematic of analog signal chain of the MPI scanner. The left side shows the transmit chain with 3rd-order band-pass filter, matching capacitances and the excitation coil while the right side shows the detection signal chain with the receive coil, a high-pass, the resonance circuit and a 2nd-order band-stop filter.

magnetic field in x -direction is ignored, thus causing image blurring. In this case, the reconstruction is used to de-blur the measured raw image.

2.3. Signal processing

The MPI scanner was tested with a spot SPION sample with $5 \mu\text{l}$ Perimag[®] stock solution, filled in a phantom with a dimension of 1.5 mm diameter in the xz plane and 3 mm length in y -direction. This phantom is placed in the center of the system. The excitation magnetic field strength is 6 mT. Figure 4(a) shows the excitation and scanning magnetic fields versus time. Note that the excitation magnetic field is applied in x -direction while the FFP is scanned in z -direction with a quasi-static scanning magnetic field H_s with a frequency of 1 Hz. It means that in 1 s the FFP is twice scanned through the FOV. A H_s strength of 17.6 mT results in a FOV of 8 mm in z -direction. For imaging in x -direction, the sample was moved by a positioning robot in the FOV in x -direction. Figure 4(b) show the measured time-domain signals without (black curve) and with (red curve) the spot SPION sample. Note that the feedthrough from the excitation magnetic field and the fundamental harmonic at frequency f_0 was eliminated digitally by a blank measurement in advance. Thus, figure 4(b) shows the time-domain signal dominated by the 3rd harmonic since other higher harmonics are filtered by the designed resonance filter. In addition, since the scanning magnetic field with 1 Hz scans the FFP in the FOV in z -direction twice, the spot SPION sample is passed with the FFP twice, thus showing time-domain signal with the same two sets (see figure 4(b)). The inset in figure 4(b) shows the zoom-in signals from the MPI scanner. Figure 4(c) shows the frequency spectra of the measured time-domain signal shown in figure 4(b). Figures 4(b) and (c) clearly show that without an SPION sample, the signal is dominated by the background noise and some residual feedthrough from the $\mu_0 H_{ac}$. Herein, the original feedthrough signal from the 3rd harmonic of the excitation magnetic field was already eliminated by a blank measurement. With an SPION sample, the 3rd harmonic was modulated by H_s , as shown in figure 4(c). Note that the inter-modulated signal shown in figure 4(c) is presented to only show the SPION magnetization and the blank signal in frequency domain. As described

in section 2.1, in a short subinterval $dt = 0.0125$ s, M_3 is calculated from the time-domain SPION magnetization shown in figure 4(b) with a digital lock-in amplifier, implemented in LabVIEW software, while the FFP position was calculated by averaging the scanning magnetic field in the same subinterval dt with given gradient magnetic fields. The maximum of the scanning magnetic field of 17.6 mT results in an FOV of 8 mm with a gradient of 4.4 T m^{-1} in z -direction. The calculated signal M_3 is depicted in figure 4(d) versus z -position, showing the 1D spatial distribution of the SPIONs. Since the FFP is scanned in z -direction twice in 1 s, it results in a voxel resolution of $2 \times 8 \text{ mm s}^{-1} \times 0.0125 \text{ s} = 0.2 \text{ mm}$.

2.4. Image reconstruction

According to the imaging concept, the single harmonic-narrowband MPI approach, presented in this paper, calculates the position of the FFP by using the gradient and scanning magnetic fields, but ignores the movement by the excitation magnetic field. To improve the spatial resolution, the raw image can be deconvoluted with the PSF or reconstructed with a measured system matrix. For the measurement of a 2D PSF, one needs to measure the 3rd harmonic signal of a spot sample while scanning the FFP through the FOV in 2D. Thus, the PSF (or system matrix) can be measured by electronically scanning the FFP through the imaging FOV, allowing fast measurements. In this paper, the PSF is measured by electrically scanning the FFP in z -direction and mechanically moved in x -direction since a scanning magnetic field coil in x -direction has not yet been implemented.

For the measurement of the PSF, a spot SPION sample with $5 \mu\text{l}$ Perimag[®] stock solution is used. Figure 5 shows the measured PSFs at different excitation magnetic fields ranging from 4 mT to 10 mT. It takes 1 s to measure the 1D PSF in z -direction and about 5 min, including mechanical scanning time, for 2D PSF with an FOV of $14 \text{ mm} \times 8 \text{ mm}$ in x - and z -direction ($71 \text{ pixels} \times 41 \text{ pixels}$). Therefore, the measurement of PSF is much less time-consuming than that in general broadband MPI.

In practice, we use a system matrix, converted from the PSF, to reconstruct the measured raw image. Figure 5(e) show the system matrix at $H_{ac} = 8 \text{ mT}$, converted from figure 5(c).

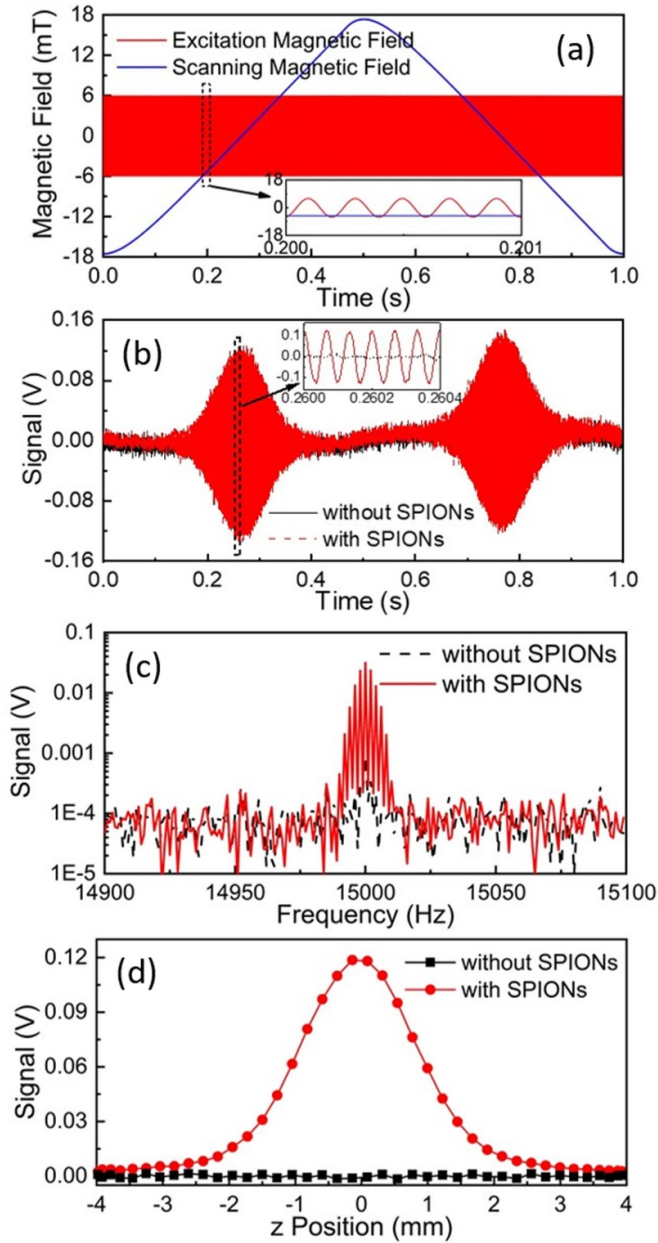


Figure 4. (a) Excitation and scanning magnetic fields in time domain. Inset shows the zoom-in signals from 0.200 to 0.201 s. (b) Time-domain signals without (black) and with (red) the spot SPION sample. Inset shows the zoom-in signals from 0.2600 to 0.2604 s. (c) The measured signals shown in (b) in frequency domain. (d) Measured 1D spatial distribution of the SPIONs, calculated from time-domain signals with a subinterval $dt = 0.0125$ s.

For reconstruction with system matrix, equation (1) can be rewritten as

$$M_3 = A \cdot c, \quad (2)$$

where A is the system matrix converted from the PSF, c is the spatial distribution of the SPION concentration, and M_3 is the measured raw image of the 3rd harmonics. In this paper, the weighted Kaczmarz method is used to solve equation (2) [53].

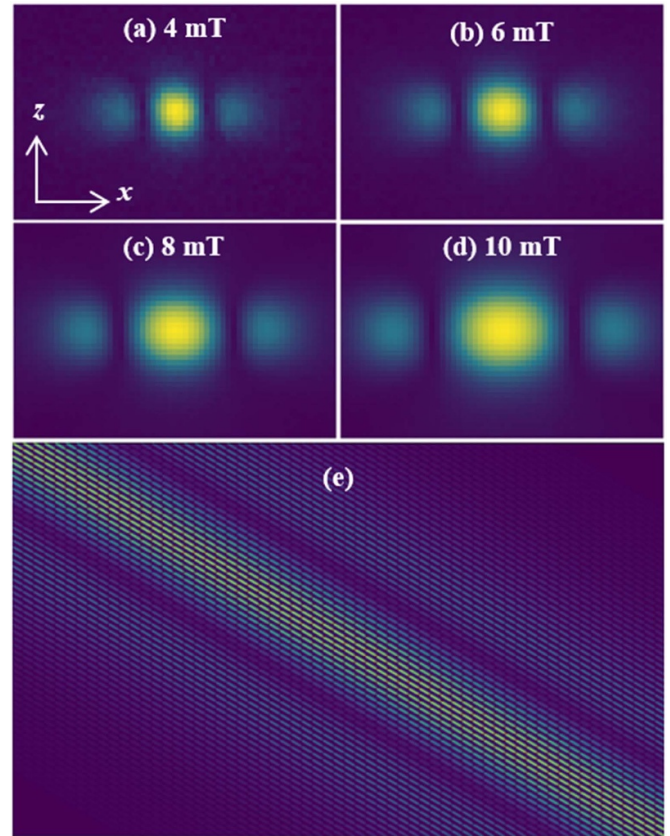


Figure 5. Measured 2D images of PSFs at different excitation magnetic fields of 4 mT (a), 6 mT (b), 8 mT (c) and 10 mT (d) in x -direction, (e) the system matrix at 8 mT. The image intensity is normalized to 1.

3. Results

3.1. Experimental description

In this paper, plain Perimag[®] SPIONs, purchased from Micro-mod GmbH (Rostock, Germany), are used as experimental sample. Perimag[®] SPIONs with a hydrodynamic diameter of about 130 nm are multi-core particles, consisting of several iron-oxide cores in a dextran matrix. The iron concentration of the stock sample is 8.5 mg ml^{-1} . In this paper, 2D images of the spatial distribution of SPIONs are measured in the xz -plane with the MPI scanner. The excitation magnetic field has a frequency of 5 kHz while the field strength is varied from 4 mT to 10 mT. The Cartesian trajectory is used for the FFP scanning with electrical scanning in z -direction and mechanical scanning in x -direction. Note that the present narrowband MPI approach only calculates the FFP position with the given gradient and scanning magnetic fields. The measurement time of one line in z -direction amounts to 1 s (1 s data acquisition). Each pixel of all the measured images has a dimension of $0.2 \text{ mm} \times 0.2 \text{ mm}$.

3.2. Spatial resolution

In this paper, the full width at half maximum (FWHM) is used to estimate the spatial resolution of the single harmonic-based

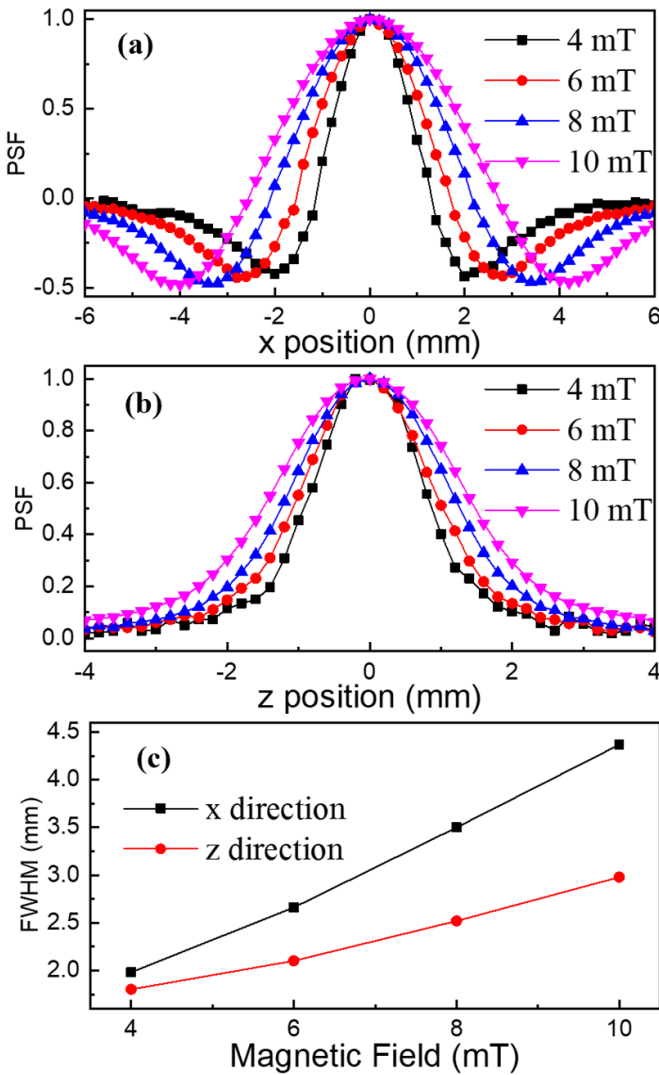


Figure 6. Figure (a) shows the normalized 1D PSF in x -direction for $z_{FFP} = 0$ (b) shows the normalized 1D PSF in z -direction for $x_{FFP} = 0$ (c) shows the dependence of the FWHMs on the amplitude of the excitation magnetic field in x - and z -direction. Symbols are experimental data whereas solid lines are guides to the eye.

narrowband MPI. Figures 6(a) and (b) show the measured 1D PSF curves in x - and z -direction at different excitation magnetic fields. To quantitatively analyze the spatial resolution, the FWHM of the PSF was calculated and presented in figure 6(c). Note that a half of the difference between the maximum and minimum values is used to calculate the FWHM. It shows that with increasing the amplitude from 4 to 10 mT, the FWHM in x -direction increases from 2.0 to 4.4 mm while the FWHM in z -direction increases from 1.8 to about 3.0 mm.

The modulation transfer function (MTF) is one of the most effective methods for the evaluation of spatial resolution. To assess the spatial resolution with MTF, different phantoms with two lines parallel to the x - and z -axis with different distances were used for experiments to calculate the MTF. Each line with a shape of a box has 1 mm width, 4 mm length in the xz plane and 3 mm depth in y -direction. Each line was filled with 12 μl Perimag[®] SPIONs. The edge-to-edge distance between the two lines was varied from 0.5 to 2 mm. Note

that in this paper the distance is calculated from edge to edge if not specified otherwise. The measured FOV amounts to 14 mm \times 8 mm in x - and z -direction. In addition, different H_{ac} from 4 to 10 mT were applied to investigate the effect of the H_{ac} strength on spatial resolution whereas the SPION concentration was varied to investigate the effect of the measurement SNR on spatial resolution. Figure 7 shows the reconstructed 2D images of the two-line phantoms filled with 8.5 mg ml⁻¹ stock suspension. It indicates that the two lines with distances of 2.0 mm and 1.5 mm can be clearly distinguished at all different H_{ac} . For line-to-line distances of 1.0 mm and 0.5 mm, the reconstructed images get blurred. The reconstructed images show that with increasing the H_{ac} , the width of the reconstructed line (1 mm) increases, which may be caused by the broader PSF at a larger H_{ac} . Note that the regularization parameter in the reconstruction with the Kaczmarz algorithm is adjusted for each measurement to provide the best image quality.

Figure 8 shows the 1D image (line) in the center of the reconstructed 2D images shown in figure 7 in x - and z -direction. The left column shows the normalized intensity versus position (intensity-position curve) in x -direction, while the right column shows it in z -direction. Each column in figure 8 shows the intensity-position curve at different H_{ac} . Based on the reconstructed 2D images shown in figure 7 and their corresponding 1D image shown in figure 8, the distinguishability of the two lines in x - and z -direction is summarized in table 1. It indicates that the two lines with distances of 2.0, 1.5 and 1.0 mm in both x - and z -direction can be distinguished at all different H_{ac} . In addition, with $\mu_0 H_{ac} = 4$ mT, the two lines with a distance of 0.5 mm in both x - and z -direction can be distinguished, indicating a spatial resolution of 0.5 mm at 4 mT. With increasing H_{ac} , the distinguishability of the two lines decreases, indicating a worse spatial resolution.

In addition, the same phantom experiments were also performed with different SPION concentrations ranging from 8.5 to 1.1 mg ml⁻¹. The reconstructed 2D images are presented in figures S1–S4 in supplementary material while the intensity-position curves are displayed in figures S5–S8, which shows similar behavior in terms of spatial resolution. In addition, they indicate that the measured images contain an increasing number of shadows/artifacts with decreasing iron concentration due to a worsened SNR. Moreover, it also becomes more difficult to distinguish the two lines from the phantom, especially with a small distance, e.g. of 0.5 mm at 4 mT. In general, the phantom experiments demonstrated that the spatial resolution in z -direction is better than that in x -direction. It is mainly caused by the higher gradient (4.4 T m⁻¹) in z -direction than that in x -direction (2.2 T m⁻¹). If only considering the gradient, the spatial resolution should be twofold better than that in x -direction. However, the spatial resolution also depends on the direction of the excitation magnetic field. The achieved spatial resolution in z -direction is slightly better than that in x -direction, not twofold better. Moreover, the spatial resolution in both x - and z -direction gets worse with increasing the excitation magnetic fields.

Based on the line phantom experiments, the MTF is calculated by using $MTF(f_{\text{spatial}}) = (c_{\text{max}} - c_{\text{min}})/(c_{\text{max}} + c_{\text{min}})$,

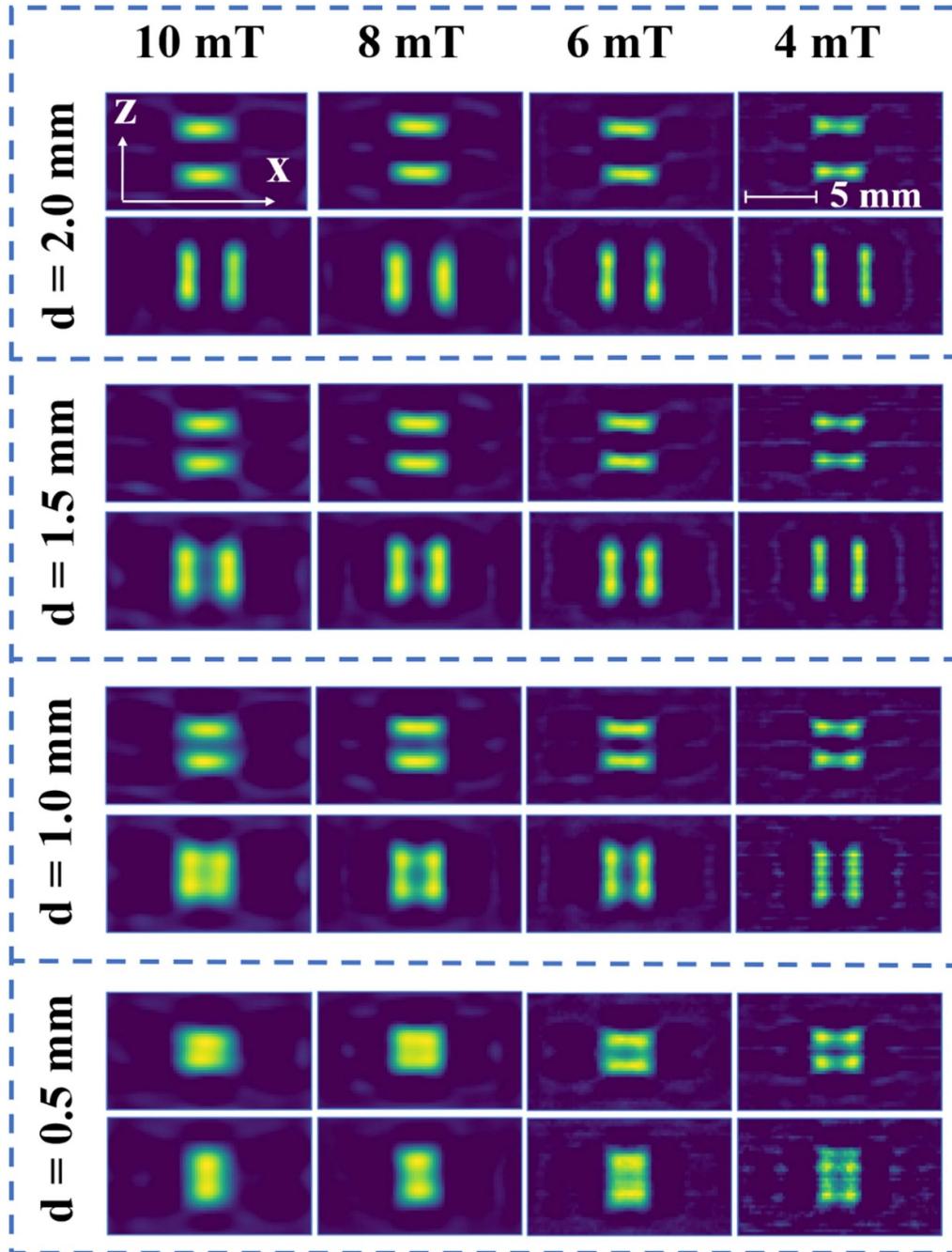


Figure 7. Reconstructed 2D images of two-line phantoms at different magnetic fields with different distances. The iron concentration is 8.5 mg ml^{-1} . The measured FOV is $14 \text{ mm} \times 8 \text{ mm}$ in x - and z -direction.

where c_{\max} (c_{\min}) is the maximum (minimum) value of the 1D curve at a given spatial frequency $f_{\text{spatial}} = 1/d$ with the edge-to-edge distance d between two lines [29, 54, 55]. Figure 9 shows the calculated MTF vs spatial frequency f_{spatial} at different $\mu_0 H_{\text{ac}}$ for different-concentration SPION samples, calculated from reconstructed images. Note that figure 9 only presents the MTFs for three different concentrations of 8.5 mg ml^{-1} , 4.3 mg ml^{-1} and 1.1 mg ml^{-1} . The spatial resolution R is defined as the value at which $\text{MTF}(1/R)$ equals 0.5. As can be seen in figure 9, with increasing the excitation magnetic field, the $1/R$ at which $\text{MTF} = 0.5$ decreases, corresponding to a worsening of the spatial resolution R with

increasing field amplitude. Figure 10 shows the calculated spatial resolution vs. the strength of the excitation magnetic field H_{ac} from the measured MTF at different SPION concentrations. It indicates that with increasing H_{ac} from 4 mT to 10 mT, the spatial resolution in x (z) varies from 0.5 mm to 1.2 mm (from 0.5 mm to 0.7 mm).

3.3. LOD

The LOD is one of the most important measures in an imaging modality. To quantitatively assess the LOD of the custom-built narrowband MPI scanner, a point phantom with 2 mm

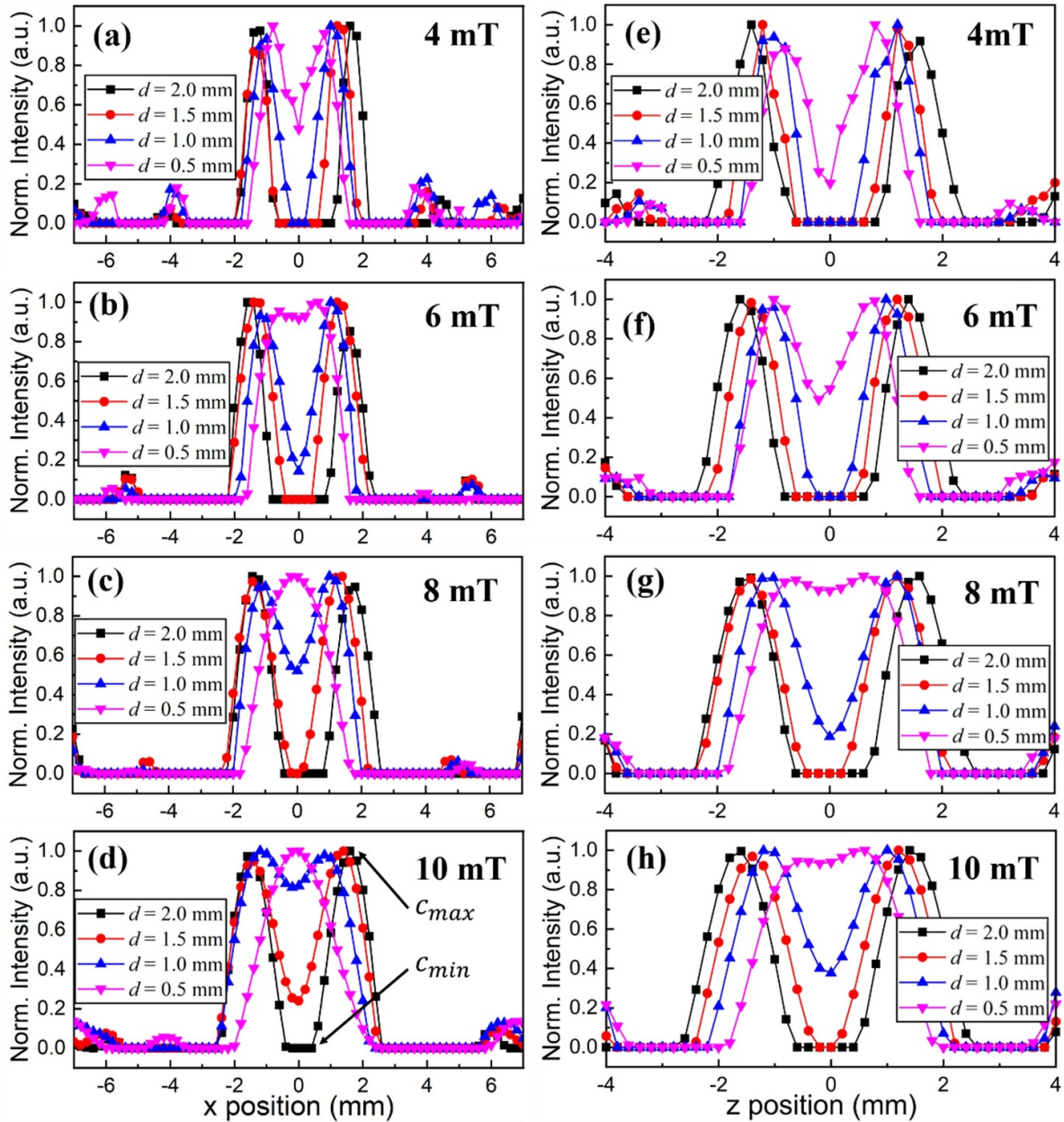


Figure 8. Experimental results of normalized image intensity vs position curves of the phantoms with 8.5 mg ml^{-1} . The left column shows the reconstructed 1D curve of normalized image intensity vs x position ($x_{\text{FFP}} = 0$), while the right column shows the reconstructed 1D curve of normalized image intensity vs z position ($x_{\text{FFP}} = 0$). The sub-figures from the 1st row to 4th rows show the measured data in different excitation magnetic fields. Symbols are experimental data whereas solid lines are guides to the eyes. In (d) an example for c_{max} and c_{min} is shown for a distance of 2 mm.

Table 1. Summary of the distinguishability of the two lines in the phantom experiments with an iron concentration of 8.5 mg ml^{-1} at different magnetic fields: distinguishable (✓) and not distinguishable (✗).

	4 mT		6 mT		8 mT		10 mT	
z	x	z	x	z	x	z	x	
$d = 0.5 \text{ mm}$	✓	✓	✗	✓	✗	✗	✗	✗
$d = 1.0 \text{ mm}$	✓	✓	✓	✓	✓	✓	✓	✓
$d = 1.5 \text{ mm}$	✓	✓	✓	✓	✓	✓	✓	✓
$d = 2.0 \text{ mm}$	✓	✓	✓	✓	✓	✓	✓	✓

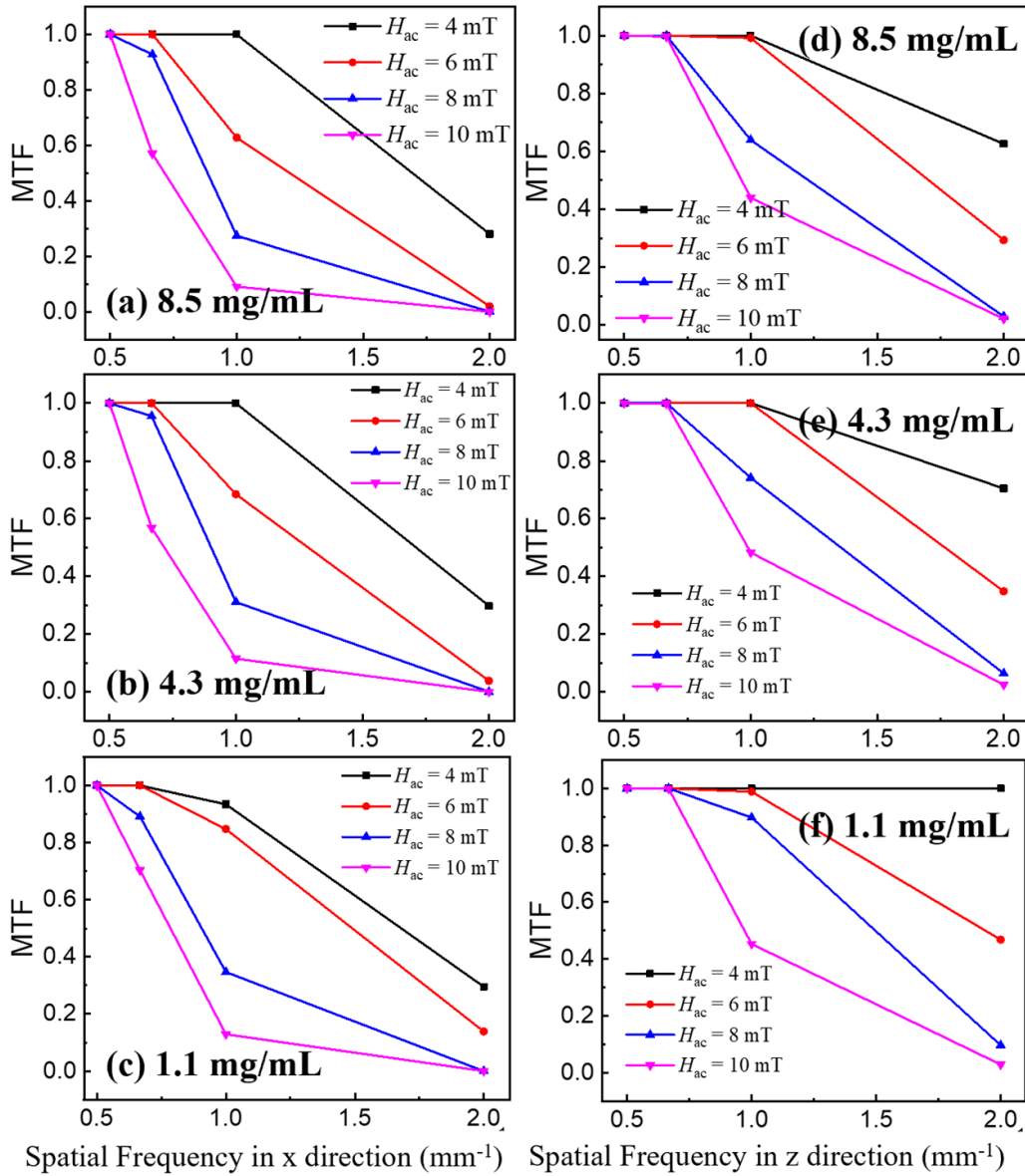


Figure 9. Experimental results of modulation transfer function in x - and z -directions at different excitation magnetic fields for three different-concentration SPION samples of 8.5 mg ml^{-1} , 4.3 mg ml^{-1} and 1.1 mg ml^{-1} .

diameter in the xz plane and 3 mm length in y direction was filled with $9.4 \mu\text{l}$ Perimag[®] SPIONs with different concentrations ranging from 8.5 mg ml^{-1} to $13 \mu\text{g ml}^{-1}$ (iron weight ranging from $80 \mu\text{g}$ to 122 ng). The phantom was imaged at different H_{ac} with a FOV of $4 \text{ mm} \times 4 \text{ mm}$ in the xz plane.

Figure 11 shows the reconstructed 2D images of the point sample. It shows that the spot sample is discernable down to $27 \mu\text{g ml}^{-1}$ at all amplitudes in the range from $\mu_0 H_{ac} = 4 \text{ mT}$ to $\mu_0 H_{ac} = 10 \text{ mT}$. However, the reconstructed image of the point sample with $27 \mu\text{g ml}^{-1}$ iron concentration at 4 mT has quite strong artifacts at the left edge. When decreasing the iron concentration from $27 \mu\text{g ml}^{-1}$ to $13 \mu\text{g ml}^{-1}$, the point phantom is not reproducibly detectable at any magnetic fields. In principle, with increasing H_{ac} to 10 mT , the 3rd harmonic gets stronger, allowing a better LOD. However, the measured/reconstructed image cannot detect the point sample.

One of the reasons may be that before the measurement of the raw image, a blank measurement of the feedthrough signal at 15 kHz due to THD should be measured. At 10 mT , the feedthrough is not very stable, thus worsening the measured raw image. Another possible reason may be that the LOD is in the range between $13 \mu\text{g ml}^{-1}$ and $27 \mu\text{g ml}^{-1}$. It is possible to detect the point sample with iron concentration of $27 \mu\text{g ml}^{-1}$ but not with iron concentration of $13 \mu\text{g ml}^{-1}$. To sum up, according to the measured and reconstructed images, the LOD of the current MPI scanner is about $27 \mu\text{g (Fe) ml}^{-1}$, corresponding to 254 ng in terms of iron weight.

3.4. Logo image

To further demonstrate the performance of the narrowband MPI, a ‘complex’ phantom—our institute logo ‘EMG’—was

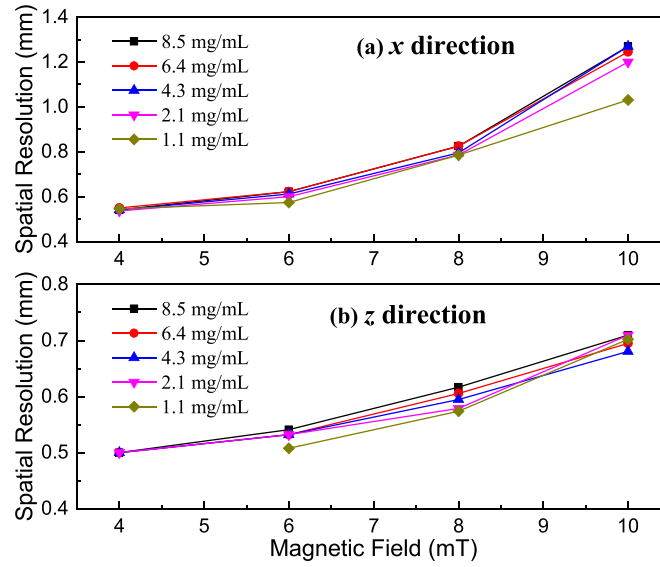


Figure 10. Spatial resolution at different magnetic fields in (a) *x*- and (b) *z*-directions, calculated from the MTF. Symbols are experimental results whereas solid lines are guide to the eye.

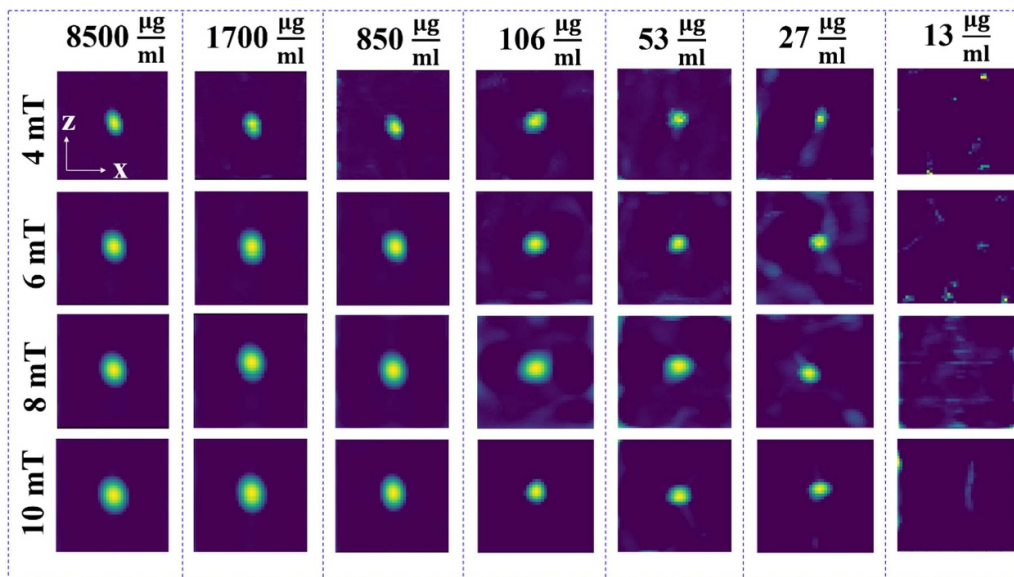


Figure 11. Reconstructed images of a point phantom with different-concentration SPION samples at different excitation magnetic fields. The reconstruction is possible down to a concentration of $27 \mu\text{g ml}^{-1}$ at all amplitudes (total amount of 254 ng iron).

filled with 8.5 mg ml^{-1} Perimag[®] SPIONs for experiments. Figure 12 shows the photo of the emg logo phantom and the reconstructed image. The imaging FOV is $34 \text{ mm} \times 10 \text{ mm}$ in *x*- and *z*-direction. Considering the spatial resolutions and the SNR at different $\mu_0 H_{ac}$, the image was measured at $\mu_0 H_{ac} = 6 \text{ mT}$. The reconstructed image, as shown in figure 12(b), can clearly resolve the designed logo. At the upper and lower edges in *z*-direction, there are some blurring in addition to the artifacts, which may come from some SPIONs at the edge (see figure 12(a)) during preparation. In addition, some signal dropout happened in the letter ‘e’ (see the white dash arrow). Nevertheless, the logo image demonstrates the feasibility of the narrowband MPI for SPION imaging.

4. Discussion

In this paper, the imaging concept of a single harmonic-based narrowband MPI is introduced. Based on the imaging concept, the narrowband MPI scanner is built to generate a scanning magnetic field for FFP movement and an excitation magnetic field for SPION excitation, as well as to only measure the 3rd harmonic of the SPIONs induced in the excitation magnetic field. The built narrowband MPI scanner uses a low-frequency scanning magnetic field for the FFP scanning in the imaging FOV and a high-frequency excitation magnetic field for the SPION excitation, instead of high-frequency and large-amplitude DFs for simultaneous FFP scanning and

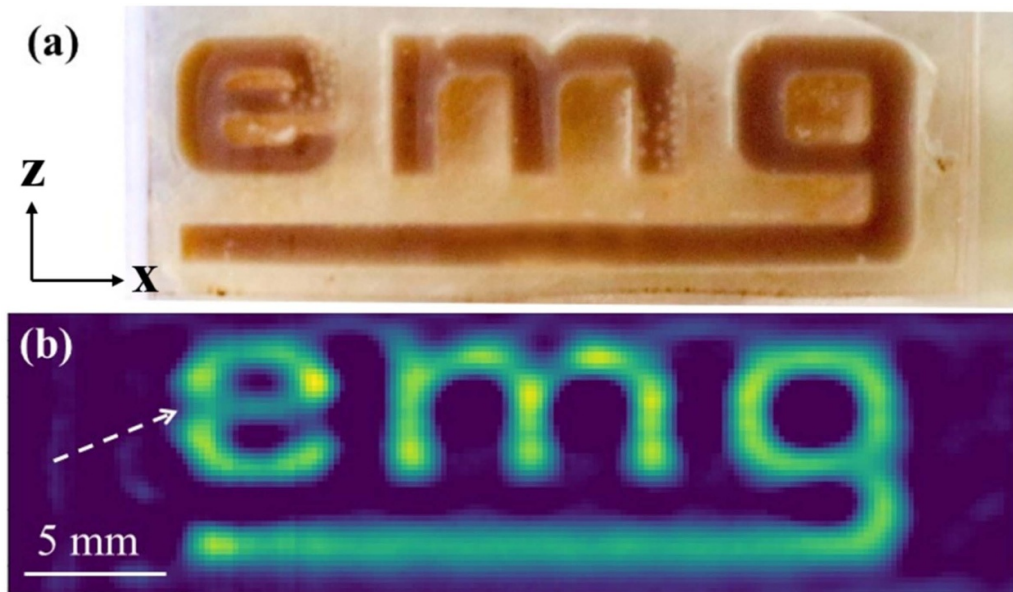


Figure 12. (a) Photo of the emg-logo phantom image filled with SPIONs. (b) Reconstructed images of the emg logo.

SPION excitation in general broadband MPI scanners. For reconstruction, the PSF or system matrix can be measured by changing the scanning magnetic fields, which significantly reduces the consumed time compared to general system matrix-based MPI approach.

The narrowband MPI scanner employed quasi-static magnetic field (1 Hz) for FFP scanning in z -direction, allowing a 1D imaging speed of 2 frames s^{-1} . Due to the low frequency, the coils for the generation of the scanning magnetic fields can be wrapped with large-diameter copper wires with a large amount turns with no needs to take into account the skin effect and self-capacitance. The THD of the scanning magnetic field does not play significant roles, but accurate measurements of the strength of the scanning magnetic fields for the calculation of the FFP position. Currently, it takes 1 s to acquire a 1D image in z -direction with the built MPI scanner. To acquire an image with a dimension of $71 \text{ pixels} \times 41 \text{ pixels}$ in xz plane, it takes about 5 min, including 71 s for data acquisition and the other extra time for mechanical scanning. By implementing the electrical scanning in x direction and increasing the frequency of the scanning magnetic field, the consuming time can be significantly reduced to a few seconds to achieve fast imaging, but not real-time imaging, similar to the superspeed-travelling wave MPI scanner ($2\text{D } 1840 \text{ frames s}^{-1}$) [56] or the commercial scanner from Bruker Biospin MRI GmbH ($3\text{D } 46 \text{ frames s}^{-1}$) [34]. Note that the FOV in the proposed narrowband MPI approach is independent of the excitation magnetic field H_{ac} . For instance, the scanning magnetic field H_s with amplitude of 17.6 mT allows an FOV of 8 mm in z -direction with the gradient magnetic field of 4.4 T m^{-1} in z -direction.

In broadband MPI scanners, the generation of the drive magnetic fields with high frequencies, e.g. 25 kHz and 45 kHz, and high amplitudes, e.g. 20 mT, is quite challenging by taking into account the THD. In the built narrowband MPI scanner,

only a 1D excitation magnetic field with a few mT amplitude, e.g. minimal 4 mT in this paper, is required to excite the SPIONs. Due to the low field strength, it is comparably easy to generate the excitation magnetic field with a nice THD. In addition, the efforts for filter design are also reduced. The built MPI scanner employs an excitation frequency of 5 kHz due to desired SPION spectra with significant contribution from Brownian relaxation. Although the 5 kHz excitation frequency is lower than that in standard broadband MPI scanners, e.g. 25 kHz, it can be simply increased by changing the impedance matching of the excitation coil and the band-pass filter on the excitation side, as well as the resonance frequency on the detection side. Therefore, the presented single harmonic-based narrowband MPI approach simplifies the MPI hardware and the implementation.

In this paper, phantom experiments indicate that the achieved spatial resolution is 0.5 mm in both x - and z -direction at $H_{ac} = 4 \text{ mT}$ with 4.4 T m^{-1} and 2.2 T m^{-1} gradients in x - and z -directions. The spatial resolutions are worsened to about 1.2 mm in x -direction and 0.7 mm in z -direction when increasing the excitation magnetic field to 10 mT. To date, the spatial resolution of MPI is in the order of sub-millimeter, depending on the gradient of the selection magnetic field and the shape of the SPION magnetization curve [29–31]. Previous studies have already demonstrated that a high spatial resolution can be achieved by decreasing the DF amplitude [36, 37, 57, 58]. The reported approach in this paper allows a better spatial resolution than that reported with the x -space MPI scanner when increasing the gradients to 6 T m^{-1} or 7 T m^{-1} , as well as other narrowband MPI approaches [39, 40]. Even compared with the approaches of pulsed and Néel-relaxation modulated MPI, the presented single harmonic-based narrowband MPI approach is comparable and promising.

In the built single harmonic-based narrowband MPI scanner, we have implemented a resonance circuit to amplify the

3rd harmonic of the SPIONs at 15 kHz. We achieve an LOD of 254 ng iron without any shielding or further efforts in the design of pre-amplifier. The currently achieved LOD is about 50 times worse than the best achieved LOD (about 5 ng iron with an acquisition time of 2.14 s) with the commercial MPI scanner from Bruker. However, there are several points that can be improved to push the LOD. The first one is that with increasing the excitation frequency from 5 kHz to 25 kHz or 45 kHz—used frequencies in the commercial MPI scanners—the LOD of the designed single-harmonic narrowband MPI scanner in principle can be further improved due to Faraday's law and high-Q in the receive coils. Secondly, we preliminarily measured the noise of our single harmonic-based narrowband MPI scanner, which mainly comes from the pre-amplifier and the external radio-wave noise. Since it has not yet been implemented with on-site shielding or in a shielding room, radio-wave noise is amplified by the resonance circuit, which also limits the LOD. An on-site shielding can be used to improve the LOD. Lastly, the used pre-amplifier was built with an AD8221 with a noise level of $8 \text{ nV Hz}^{-1/2}$. Since the detection coil works at a resonance frequency of 15 kHz, the impedance of the receive side is very high in the order of 10 k Ω . The noise of the pre-amplifier—about $50 \text{ nV Hz}^{-1/2}$ —comes from both current and voltage noise. With further improvement in the pre-amplifier, we believe that the noise of the pre-amplifier can be improved down to $1 \text{ nV Hz}^{-1/2}$ by a factor of around 50. Based on the statements above on an increase in excitation frequency, implementation of shielding and pre-amplifier improvement, we believe that the LOD may be improved to the order of 5 ng iron mass.

Considering all the factors involved in MPI, e.g. hardware design efforts, spatial resolution, sensitivity and safety, the single-harmonic-based narrowband MPI presented in this paper is a very promising approach to reach a good trade-off in spatial resolution and LOD without bringing significant issues in safety.

5. Conclusion

In this paper, we systematically investigated a single-harmonic based narrowband MPI. The concept of the narrowband MPI was introduced while the single harmonic-based narrowband MPI scanner was built to visualize the spatial distributions of SPIONs. Different phantom experiments were performed to demonstrate the feasibility of the narrowband MPI for SPION concentration imaging. In addition, FWHM and MTF were measured and used as different metrics to comprehensively evaluate the spatial resolution, as well as its dependence on the strength of excitation magnetic field. The LOD of the custom-built MPI scanner was determined based on images of phantoms with SPIONs with different concentrations. The proposed narrowband MPI approach simplifies the MPI scanner design and the measurement of PSF and system matrix, but still allows good performance in terms of spatial resolution and LOD. We envisage that the present methodology is an alternative MPI approach, showing promising performance in terms of spatial resolution and LOD. We believe that our study

is of great interest and importance to biomedicines, including molecular imaging, cell tracking and targeted drug delivery.

Data availability statement

All data that support the findings of this study are included within the article (and any supplementary files).

Acknowledgments

The financial supports from German Research Foundation (DFG) under Grant ZH 782/1-1 and the National Key R&D Program of China under Grant 2019YFB1309700 are gratefully acknowledged.

ORCID iDs

Klaas-Julian Janssen  <https://orcid.org/0000-0003-0575-893X>

Jing Zhong  <https://orcid.org/0000-0002-8815-4105>

References

- [1] Hultman K L, Raffo A J, Grzenda A L, Harris P E, Brown T R and O'Brien S 2008 Magnetic resonance imaging of major histocompatibility class II expression in the renal medulla using immunotargeted superparamagnetic iron oxide nanoparticles *ACS Nano* **2** 477–84
- [2] Shevtsov M A *et al* 2015 Ionizing radiation improves glioma-specific targeting of superparamagnetic iron oxide nanoparticles conjugated with cmHsp70.1 monoclonal antibodies (SPION–cmHsp70.1) *Nanoscale* **7** 20652–64
- [3] Shevtsov M A, Nikolaev B P, Yakovleva L Y, Marchenko Y Y, Dobrodumov A V, Mikhrina A L, Martynova M G, Bystrova O A, Yakovenko I V and Ischenko A M 2014 Superparamagnetic iron oxide nanoparticles conjugated with epidermal growth factor (SPION–EGF) for targeting brain tumors *Int. J. Nanomed.* **9** 273
- [4] Briley-Saebo Karen C, Cho Young S, Shaw Peter X, Ryu Sung K, Mani V, Dickson S, Izadmehr E, Green S, Fayad Zahi A and Tsimikas S 2011 Targeted iron oxide particles for *in vivo* magnetic resonance detection of atherosclerotic lesions with antibodies directed to oxidation-specific epitopes *J. Am. Coll. Cardiol.* **57** 337–47
- [5] Chilkoti A, Dreher M R, Meyer D E and Raucher D 2002 Targeted drug delivery by thermally responsive polymers *Adv. Drug Deliv. Rev.* **54** 613–30
- [6] Alexiou C, Diehl D, Henninger P, Iro H, Rockelein R, Schmidt W and Weber H 2006 A high field gradient magnet for magnetic drug targeting *IEEE Trans. Appl. Supercond.* **16** 1527–30
- [7] Alexiou C, Arnold W, Klein R J, Parak F G, Hulin P, Bergemann C, Erhardt W, Wagenpfeil S and Lübke A S 2000 Locoregional cancer treatment with magnetic drug targeting *Cancer Res.* **60** 6641–8
- [8] Jordan A, Scholz R, Wust P, Fähling H and Felix R 1999 Magnetic fluid hyperthermia (MFH): cancer treatment with AC magnetic field induced excitation of biocompatible superparamagnetic nanoparticles *J. Magn. Magn. Mater.* **201** 413–9
- [9] Rosensweig R E 2002 Heating magnetic fluid with alternating magnetic field *J. Magn. Magn. Mater.* **252** 370–4

- [10] Huang G, Gao J, Hu Z, John J V S, Ponder B C and Moro D 2004 Controlled drug release from hydrogel nanoparticle networks *J. Control. Release* **94** 303–11
- [11] Liu T Y, Liu K H, Liu D M, Chen S Y and Chen I W 2009 Temperature-sensitive nanocapsules for controlled drug release caused by magnetically triggered structural disruption *Adv. Funct. Mater.* **19** 616–23
- [12] Ahrens E T and Bulte J W M 2013 Tracking immune cells *in vivo* using magnetic resonance imaging *Nat. Rev. Immunol.* **13** 755–63
- [13] Perrin J et al 2020 Cell tracking in cancer immunotherapy *Front. Med.* **7** 34
- [14] Ni J-S, Li Y, Yue W, Liu B and Li K 2020 Nanoparticle-based cell trackers for biomedical applications *Theranostics* **10** 1923
- [15] Sanz-Ortega L, Rojas J M, Marcos A, Portilla Y, Stein J V and Barber D F 2019 T cells loaded with magnetic nanoparticles are retained in peripheral lymph nodes by the application of a magnetic field *J. Nanobiotechnol.* **17** 1–20
- [16] Sharkey J et al 2017 Functionalized superparamagnetic iron oxide nanoparticles provide highly efficient iron-labeling in macrophages for magnetic resonance-based detection *in vivo* *Cytotherapy* **19** 555–69
- [17] Gleich B and Weizenecker J 2005 Tomographic imaging using the nonlinear response of magnetic particles *Nature* **435** 1214–7
- [18] Knopp T, Gdaniec N and Möddel M 2017 Magnetic particle imaging: from proof of principle to preclinical applications *Phys. Med. Biol.* **62** R124
- [19] Goodwill P W and Conolly S M 2010 The x-space formulation of the magnetic particle imaging process: 1-D signal, resolution, bandwidth, SNR, SAR, and magnetostimulation *IEEE Trans. Med. Imaging* **29** 1851–9
- [20] Goodwill P W, Konkle J J, Zheng B, Saritas E U and Conolly S M 2012 Projection x-space magnetic particle imaging *IEEE Trans. Med. Imaging* **31** 1076–85
- [21] Goodwill P W and Conolly S M 2011 Multidimensional x-space magnetic particle imaging *IEEE Trans. Med. Imaging* **30** 1581–90
- [22] Vogel P, Rückert M A, Klauer P, Kullmann W H, Jakob P M and Behr V C 2013 Traveling wave magnetic particle imaging *IEEE Trans. Med. Imaging* **33** 400–7
- [23] Gräfe K, von Gladiss A, Bringout G, Ahlborg M and Buzug T M 2015 2D images recorded with a single-sided magnetic particle imaging scanner *IEEE Trans. Med. Imaging* **35** 1056–65
- [24] Sattel T F, Knopp T, Biederer S, Gleich B, Weizenecker J, Borgert J and Buzug T M 2008 Single-sided device for magnetic particle imaging *J. Phys. D: Appl. Phys.* **42** 022001
- [25] Bente K, Weber M, Graeser M, Sattel T F, Erbe M and Buzug T M 2014 Electronic field free line rotation and relaxation deconvolution in magnetic particle imaging *IEEE Trans. Med. Imaging* **34** 644–51
- [26] Top C B and Gungör A 2020 Tomographic field free line magnetic particle imaging with an open-sided scanner configuration *IEEE Trans. Med. Imaging* **39** 4164–73
- [27] Weizenecker J, Gleich B, Rahmer J, Dahnke H and Borgert J 2009 Three-dimensional real-time *in vivo* magnetic particle imaging *Phys. Med. Biol.* **54** L1
- [28] Vogel P, Rückert M A, Kampf T, Herz S, Stang A, Wöckel L, Bley T A, Dutz S and Behr V C 2020 Superspeed bolus visualization for vascular magnetic particle imaging *IEEE Trans. Med. Imaging* **39** 2133–9
- [29] Knopp T, Biederer S, Sattel T F, Erbe M and Buzug T M 2011 Prediction of the spatial resolution of magnetic particle imaging using the modulation transfer function of the imaging process *IEEE Trans. Med. Imaging* **30** 1284–92
- [30] Arami H, Teeman E, Troksa A, Bradshaw H, Saatchi K, Tomitaka A, Gambhir S S, Häfeli U O, Liggitt D and Krishnan K M 2017 Tomographic magnetic particle imaging of cancer targeted nanoparticles *Nanoscale* **9** 18723–30
- [31] Tay Z W, Hensley D, Ma J, Chandrasekharan P, Zheng B, Goodwill P and Conolly S 2019 Pulsed excitation in magnetic particle imaging *IEEE Trans. Med. Imaging* **38** 2389–99
- [32] Tay Z W, Savliwala S, Hensley D W, Fung K B, Colson C, Fellows B D, Zhou X, Huynh Q, Lu Y and Zheng B 2021 Superferromagnetic nanoparticles enable order-of-magnitude resolution and sensitivity gain in magnetic particle imaging *Small Methods* **5** 2100796
- [33] Goodwill P W, Scott G C, Stang P P and Conolly S M 2009 Narrowband magnetic particle imaging *IEEE Trans. Med. Imaging* **28** 1231–7
- [34] Graeser M, Knopp T, Szargulski P, Friedrich T, von Gladiss A, Kaul M, Krishnan K M, Itrich H, Adam G and Buzug T M 2017 Towards picogram detection of superparamagnetic iron-oxide particles using a gradiometric receive coil *Sci. Rep.* **7** 6872
- [35] Saritas E U, Goodwill P W, Zhang G Z and Conolly S M 2013 Magnetostimulation limits in magnetic particle imaging *IEEE Trans. Med. Imaging* **32** 1600–10
- [36] Croft L R, Goodwill P W, Konkle J J, Arami H, Price D A, Li A X, Saritas E U and Conolly S M 2016 Low drive field amplitude for improved image resolution in magnetic particle imaging *Med. Phys.* **43** 424–35
- [37] Weber A, Weizenecker J, Rahmer J, Franke J, Heinen U and Buzug T M 2015 Resolution improvement by decreasing the drive field amplitude *Int. Workshop on Magnetic Particle Imaging (Istanbul, Turkey, March 26–28)* (<https://doi.org/10.1109/IWMPI.2015.7107020>)
- [38] Bai S, Hirokawa A, Tanabe K, Sasayama T, Yoshida T and Enpuku K 2015 Narrowband magnetic particle imaging utilizing electric scanning of field free point *IEEE Trans. Magn.* **51** 5300105
- [39] Tanaka S, Murata H, Oishi T, Hatsukade Y, Zhang Y, Horng H-E, Liao S-H and Yang H-C 2015 Imaging of magnetic nanoparticles using a second harmonic of magnetization with DC bias field *IEEE Trans. Magn.* **51** 5300105
- [40] Pi S, Liu W and Jiang T 2018 Real-time and quantitative isotropic spatial resolution susceptibility imaging for magnetic nanoparticles *Meas. Sci. Technol.* **29** 035402
- [41] Jiang T, Pi S, Shi J, Zhang P, Liu W and Cheng J 2019 Influence of signal bandwidth and phase delay on complex susceptibility based magnetic particle imaging *Meas. Sci. Technol.* **30** 115401
- [42] Le T-A, Zhang X, Hoshier A K and Yoon J 2017 Real-time two-dimensional magnetic particle imaging for electromagnetic navigation in targeted drug delivery *Sensors* **17** 2050
- [43] Murase K, Hiratsuka S, Song R and Takeuchi Y 2014 Development of a system for magnetic particle imaging using neodymium magnets and gradiometer *Jpn. J. Appl. Phys.* **53** 067001
- [44] Trisnanto S B and Takemura Y 2019 Modulating relaxation responses of magnetic nanotracers for submillimeter imaging *Appl. Phys. Lett.* **115** 123101
- [45] Zhong J, Schilling M and Ludwig F 2018 Magnetic nanoparticle temperature imaging with a scanning magnetic particle spectrometer *Meas. Sci. Technol.* **29** 115903
- [46] Richter H, Kettering M, Wiekhorst F, Steinhoff U, Hilger I and Trahms L 2010 Magnetorelaxometry for localization and

- quantification of magnetic nanoparticles for thermal ablation studies *Phys. Med. Biol.* **55** 623
- [47] Fodil K, Denoual M and Dolabdjian C 2015 Experimental and analytical investigation of a 2D magnetic imaging method using magnetic nanoparticles *IEEE Trans. Magn.* **52** 5300105
- [48] Schilling M, Ludwig F, Kuhlmann C and Wawrzik T 2013 Magnetic particle imaging scanner with 10-kHz drive-field frequency *Biomed. Eng.* **58** 557–63
- [49] Mason E, Cooley C, Cauley S, Griswold M, Conolly S and Wald L 2017 Design analysis of an MPI human functional brain scanner *Int. J. Magn. Part. Imaging* (<https://doi.org/10.18416/ijmpi.2017.1703008>)
- [50] Mason E, Mattingly E, Herb K, Sliwiak M, Franconi S, Cooley C, Slanetz P and Wald L 2021 Concept for using magnetic particle imaging for intraoperative margin analysis in breast-conserving surgery *Sci. Rep.* **11** 13456
- [51] Tonyushkin A, Chinchilla C, McDonough C, Negash A and Pagan J 2021 2D projection image reconstruction for field free line single-sided magnetic particle imaging scanner: simulation studies *Int. J. Magn. Part. Imaging* (<https://doi.org/10.18416/ijmpi.2021.2104001>)
- [52] Pagan J, McDonough C, Vo T and Tonyushkin A 2021 Single-sided magnetic particle imaging device with field-free-line geometry for *in vivo* imaging applications *IEEE Trans. Magn.* **57** 5300105
- [53] Knopp T, Rahmer J, Sattel T, Biederer S, Weizenecker J, Gleich B, Borgert J and Buzug T 2010 Weighted iterative reconstruction for magnetic particle imaging *Phys. Med. Biol.* **55** 1577
- [54] Judy P F 1976 The line spread function and modulation transfer function of a computed tomographic scanner *Med. Phys.* **3** 233–6
- [55] Zhong J, Schilling M and Ludwig F 2018 Spatial and temperature resolutions of magnetic nanoparticle temperature imaging with a scanning magnetic particle spectrometer *Nanomaterials* **8** 866
- [56] Vogel P, Rückert M, Klauer P, Kullmann W, Jakob P and Behr V 2015 Superspeed travelling wave magnetic particle imaging *IEEE Trans. Magn.* **51** 6501603
- [57] TOP C B 2020 An arbitrary waveform magnetic nanoparticle relaxometer with an asymmetrical three-section gradiometric receive coil *Turk. J. Electr. Eng. Comput. Sci.* **28** 1344–54
- [58] Tay Z W, Hensley D W, Chandrasekharan P, Zheng B and Conolly S M 2019 Optimization of drive parameters for resolution, sensitivity and safety in magnetic particle imaging *IEEE Trans. Med. Imaging* **39** 1724–34